JACS
JOURNAL OF THE AMERICAN CHEMICAL SOCIETY
pubs.acs.org/JACS
Article

In Situ Characterization of Dehydration during Ion Transport in Polymeric Nanochannels

Chenghai Lu, Chengzhi Hu,* Cody L. Ritt, Xin Hua, Jingqiu Sun, Hailun Xia, Yingya Liu, Da-Wei Li, Baiwen Ma, Menachem Elimelech,* and Jiuhui Qu*

Cite This: *J. Am. Chem. Soc.* 2021, 143, 14242−14252

Read Online

ACCESS | Metrics & More | Article Recommendations | Supporting Information

ABSTRACT: The transport of hydrated ions across nanochannels is central to biological systems and membrane-based applications, yet little is known about their hydrated structure during transport due to the absence of *in situ* characterization techniques. Herein, we report experimentally resolved ion dehydration during transmembrane transport using modified *in situ* liquid ToF-SIMS in combination with MD simulations for a mechanistic reasoning. Notably, complete dehydration was not necessary for transport to occur across membranes with sub-nanometer pores. Partial shedding of water molecules from ion solvation shells, observed as a decrease in the average hydration number, allowed the alkali-metal ions studied here (lithium, sodium, and potassium) to permeate membranes with pores smaller than their solvated size. We find that ions generally cannot hold more than two water molecules during this sterically limited transport. In nanopores larger than the size of the solvation shell, we show that ionic mobility governs the ion hydration number distribution. Viscous effects, such as interactions with carboxyl groups inside the membrane, preferentially hinder the transport of the mono- and dihydrates. Our novel technique for studying ion solvation *in situ* represents a significant technological leap for the nanofluidics field and may enable important advances in ion separation, biosensing, and battery applications.

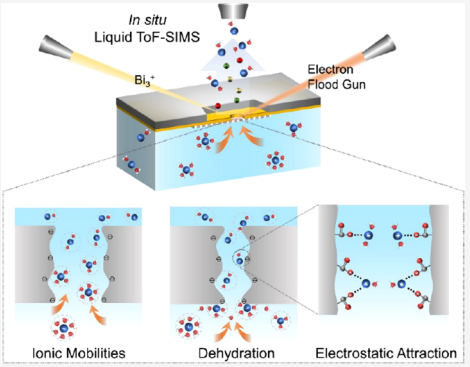

INTRODUCTION

The transport of hydrated ions through nanochannels is ubiquitous in nature as well as in many industrial and biomedical applications.[1−4] Due to magnified interactions with pore walls under extreme confinement,[5,6] the phenomenological behavior and properties of confined ions deviate from those of their bulk solution state. Biological[1,4,7] and artificial[3,8−12] nanochannels capable of ultraprecise sensing and ion separation frequently exploit this phenomenon by balancing the energetic penalties and compensation associated with ion−pore interactions for target species.[13] Ion dehydration and viscous effects are two prominent mechanisms that often contribute to an ion's energy barrier,[13,14] which has recently been shown in simulations on graphene nanochannels.[15,16] In brief, energetically unfavorable shedding and rearrangement of an ion's solvation shell—termed dehydration—must occur for the ion to access a confined space. Once inside, viscous effects arising from attractive or repulsive interactions between the ion and functional groups decorating the pore wall can subsequently increase or offset the energetic penalties incurred from dehydration,[17,18] consequently hindering or promoting the diffusion inside the pore.

Despite the prominence of this transport process, there remains much to be discovered about the mechanisms of ion transport under confinement. Numerous theoretical simulations suggest that ion dehydration is central to transport across single-digit and sub-nanometer pores and that it can be affected by the size, shape, and binding energy of the solvation shell.[4,11,19] However, *in situ* experimental investigations have thus far eluded researchers. Improving our understanding of these nanofluidic transport mechanisms holds substantial scientific value and would enable improved designs for processes related to ion separation, clean energy conversion, and biomedicines.[7,20−22] In the case of ion separation, developing membranes with nanopores tailored to match the ion solvation structure could significantly enhance ion−ion selectivity and lead to increased energy and process efficiencies.[13,23] Elucidating the dynamic structural transformation of hydrated ions during nanoconfined transport is therefore paramount for achieving these desired molecular-level designs.

Due to spatial and temporal limitations, conventional experimental techniques using infrared (IR),[24] nuclear

Received: June 3, 2021
Published: August 25, 2021

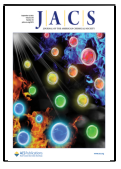

https://doi.org/10.1021/jacs.1c05765
J. Am. Chem. Soc. 2021, 143, 14242−14252

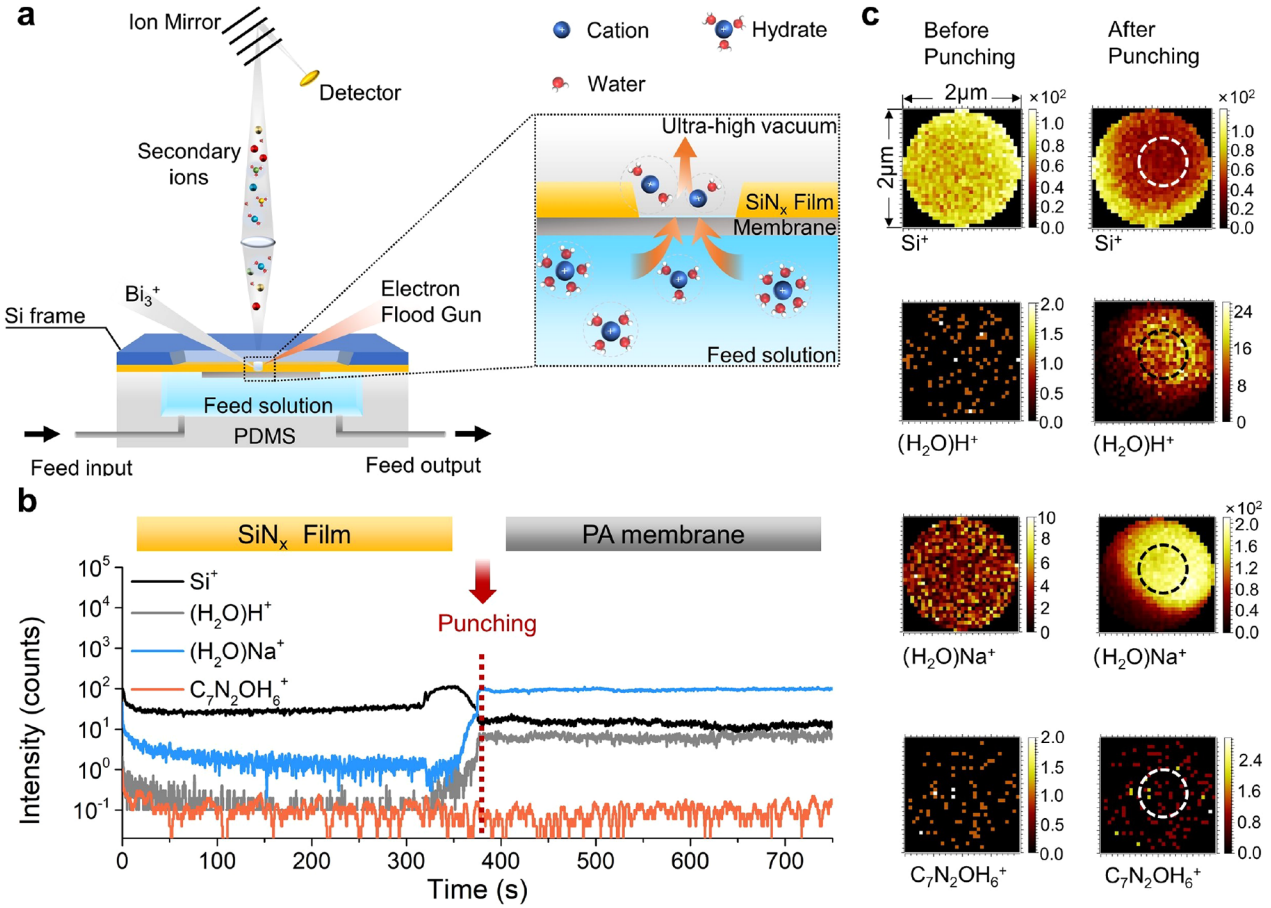

Figure 1. *In situ* discrimination of h_{I^+} distribution during transmembrane ion transport. (a) Schematic illustration of the *in situ* liquid ToF-SIMS analysis combined with a microfluidic nanofiltration platform. (b) Dynamic ToF-SIMS depth profiling of Si^+, $(H_2O)H^+$, $(H_2O)Na^+$, and $C_7N_2OH_6^+$. The SiN_x film was punched through around 375 s, allowing NaCl to permeate the polyamide membrane. The data were collected from filtration of 1 mM NaCl at pH 6.5 by an NF90 membrane. The dashed line in the center represents the time scales of data acquisition. (c) Reconstructed 2D chemical images of Si^+, $(H_2O)H^+$, $(H_2O)Na^+$, and $C_7N_2OH_6^+$ before and after perforation of the SiN_x film. A lighter color represents a stronger signal intensity. The dotted circle represents the region of interest (ROI) of mass spectrum signals selected for an h_{I^+} distribution analysis.

magnetic resonance (NMR),[25] X-ray diffraction (XRD),[26] vibrational sum frequency spectroscopy (VSFS),[27] and extended X-ray absorption fine structure (EXAFS)[28] lack the ability to provide dynamic and instantaneous information regarding an ion's solvated structure during confined transport. Consequently, there is sparse experimental data supporting our present understanding of confinement effects on ion dehydration. Time-of-flight secondary ion mass spectrometry (ToF-SIMS) is a highly sensitive mass-spectrometric technique for surface/interface analysis with high spatial resolution that offers a potential solution.[29−32] Recently, *in situ* liquid ToF-SIMS was developed by combining ToF-SIMS with novel microfluidic chip designs as a soft-ionization technique to realize *operando* discrimination of various ion−solvent interactions and properties, including ion solvation numbers (h_I) in aqueous and nonaqueous solutions.[31,33,34]

Herein, we report a systematic study of confinement-induced ion dehydration and transport by leveraging a modified *in situ* liquid ToF-SIMS microfluidic filtration platform. Our microfluidic apparatus is tailored for analyzing ion dehydration and transport in polyamide-based nanofiltration membranes with sub-nanometer pores. We assess how physicochemical properties influence the dehydration and viscous effects during monovalent cation transport by studying the distribution of h_{I^+} in polyamide membranes of various pore sizes and chemical functionalities. We observe confinement-induced partial dehydration of the ion solvation shells during the transport of lithium, sodium, and potassium ions. In nanopores larger than the size of the solvation shell, we find that ionic mobility has an outsized effect on the distribution of h_{I^+}. Viscous effects, such as interactions with carboxyl groups within the membrane pore channel, are found to hinder transport of the partially hydrated ions. Our novel experimental technique for studying *in situ* ion solvation represents a significant technological advance that will enable researchers to elucidate mechanisms underlying confined ion transport. Such an advancement could have significant implications for applications that commonly exploit confined transport, such as desalination, biosensing, and battery storage.

RESULTS AND DISCUSSION

Dehydration of Sodium Ions during Transmembrane Transport. We fabricated a microfluidic filtration platform for an *in situ* ToF-SIMS analysis (see the Experimental Section), where a polyamide membrane was sealed between an electrolyte solution and a SiN_x film with epoxy glue. The membrane was exposed to an electrolyte feed solution via injection into a polydimethylsiloxane (PDMS) reservoir prior

https://doi.org/10.1021/jacs.1c05765
J. Am. Chem. Soc. 2021, 143, 14242−14252

to punching the SiN_x film with a pulsed Bi_3^+ primary ion beam. Water and ion transport were driven across the membrane by pulling an ultrahigh vacuum at the membrane surface, consequently exposing the Bi_3^+ beam to a stable liquid−vacuum interface confined within an ∼2 μm detection area (Figure S1). The experimental design is illustrated in Figure 1a. Secondary ions produced by bombarding the permeate with Bi_3^+ were available for instantaneous mass spectrum analysis.

The dramatic decrease in the Si^+ signal intensity indicates that the SiN_x film was completely punched through after ∼375 s of Bi_3^+ exposure (Figure 1b). Simultaneous increases in the $(H_2O)Na^+$ and $(H_2O)H^+$ signals, corresponding to hydrated sodium and protonated water clusters, respectively, further support successful perforation of the SiN_x film at this time stamp. No obvious signals from peaks characteristic of the polyamide membrane ($C_7N_2OH_6^+$)[35,36] were observed during the ToF-SIMS analysis, suggesting that the polyamide membrane maintained its structural integrity during the sample measurement (more details of the dynamic depth profile can be found in Figure S2). Reconstructed chemical mapping of the *in situ* detection area (Figure 1c; details are given in the Supporting Information) reveals the nanometer-scale spatial resolution of ToF-SIMS. Moreover, reconstructed chemical mapping before and after perforation of the SiN_x film (Figure 1c) match the transitions in signals observed in the dynamic depth profiling (Figure 1b). These results indicate that *in situ* liquid ToF-SIMS can be used during the nanofiltration operation to attain instantaneous mass information on the permeate.

By normalizing the mass spectrum peak intensities of individual hydrates obtained from ToF-SIMS to the total hydrated ion mass spectrum, we can determine the distribution of h_{I^+} under confinement (Figure S3; details are given in the Supporting Information). We evaluated the hydration number distribution of sodium (h_{Na+}) in 10 mM NaCl before and after filtration by the NF90 membrane (Figure 2a). In bulk solution (i.e., before filtration), h_{Na+} shows a normal-like distribution with the highest proportion of trihydrates, $(H_2O)_3Na^+$, over other hydration species (i.e., $(H_2O)_nNa^+$ with $n = 1-6$). The results indicate an average h_{Na+} value of 3.03 water molecules. This value is lower than values found in previous diffraction studies and molecular dynamics simulations, where h_{Na+} values are often reported between 4 and 8.[37,38] These methods, however, are based on the geometry of the solvent molecules that accommodate the ion, whether strongly bound or not.[39] Theoretical extractions of h_{Na+} from measurable bulk properties, such as electrostriction of water by the electric field of the ion,[39,40] ionic compressibility,[41,42] entropy of hydration,[39] and ionic size,[39,42] display average h_{Na+} values ranging from 2.9 to 4.5—in good agreement with our results. The principal difference between h_{Na+} values determined by the geometric methods and theoretical extractions is the nature of the solvent binding. Elucidating h_{Na+} via theoretical extraction pertains only to solvent molecules strongly bound to the ion so that they move along with it in solution.[39] We thus posit that h_{I^+} determined by ToF-SIMS refers primarily to water molecules bound to the ion by its strong Coulombic field (additional discussion is given in the Supporting Information).

Filtering the feed solution through NF90, a commercial polyamide-based nanofiltration membrane with sub-nanometer pores,[43] led to a right-skewed h_{Na+} distribution (Figure 2a). Larger hydrates (i.e., $(H_2O)_nNa^+$ with $n \geq 3$) became significantly diminished while smaller hydrates (i.e., $(H_2O)_nNa^+$ with $n < 3$) became more prevalent. In particular, dihydrates became the dominant hydration species, leading to an average h_{Na+} value of 1.86 water molecules. Coinciding with the observed decrease of more than one water molecule in the average size of the strongly bound solvation shell, we find that the proportion of larger hydrates ($\chi_{n\geq 3}$), defined here as $\sum(H_2O)_{n\geq 3}Na^+/\sum(H_2O)_nNa^+$, shifts from 0.63 to 0.07 after permeating across the sub-nanometer pores of the membrane. The same trends were observed in 1 mM NaCl solution as well (Figure S4).

The solution pH, which varies for many aqueous media of biological and industrial relevance, also plays a critical role in local and long-range ion−water interactions.[24,44] It is thus reasonable to expect the solution pH to influence the structure and size of solvated ions.[24,44−46] While we find no significant difference between the bulk h_{Na+} distributions at pH 6.5 (Figure 2a) and pH 3 (Figure 2b), a substantial shift was observed when the pH was increased to 11 (Figure 2b). The increase in pH caused a dominant hydration species transition from trihydrate to monohydrate in the bulk solution, subsequently decreasing the average h_{Na+} value from 3.03 to 2.38 water molecules. In fact, the proportion of all larger hydrates (i.e., $\chi_{n\geq 3}$) decreased at higher pH. Due to the important role of electrostatics in ion−water interactions,[39] we postulate that higher OH^- concentrations may have induced charge shielding and consequently reduced the effective charge density of sodium ions.[44] The reduction in the average h_{Na+} value at pH 11 is thus likely attributed to a weakened electrostatic attraction between the sodium ions and the surrounding water molecules.

The h_{Na+} distributions were nearly identical for all feed solution pH values after filtration (Figure 2a,b and Figure S4). The disappearance of larger hydrates could be explained by their inability to enter the sub-nanometer pores, forcing the sodium ions to partially dehydrate to the smaller hydrate species.[47,48] The pH independence of the h_{Na+} distributions post-filtration could also be due to lower local proton concentrations within the nanoporous polyamide film. This phenomenon is common in ion exchange resins[49] and appears to be plausible for polyamide films.[50,51] Lower local proton concentrations within the active layer would mean that the pH experienced by sodium ions during transmembrane transport would be significantly lower than what is measured in the bulk solution. This would likely negate the charge-shielding effects observed in the high-pH bulk solution.

Notably, we find a transition in the proportion of dihydrate to monohydrate species, $\chi_{n=2}/\chi_{n=1}$, after filtration for all conditions (Figure S5). The disparity in $\chi_{n=2}/\chi_{n=1}$ before and after filtration under the various conditions indicates that dehydration is not merely driven by the complete exclusion of larger sodium hydrates from the membrane; rather, a partial dehydration-driven transformation is occurring. In other words, our data suggest that large sodium hydrates are reducing their effective size by shedding part of their solvation shell to partition into and permeate across the sub-nanometer polyamide pores. Partial dehydration has been observed previously *in silico*,[52] but this is, to our knowledge, the first account of this phenomenon being evidenced *in situ* during transmembrane transport. Our results indicate that (i) sodium ions are unlikely to carry more than two strongly bound water molecules during transport across the nanoporous NF90

https://doi.org/10.1021/jacs.1c05765
J. Am. Chem. Soc. 2021, 143, 14242−14252

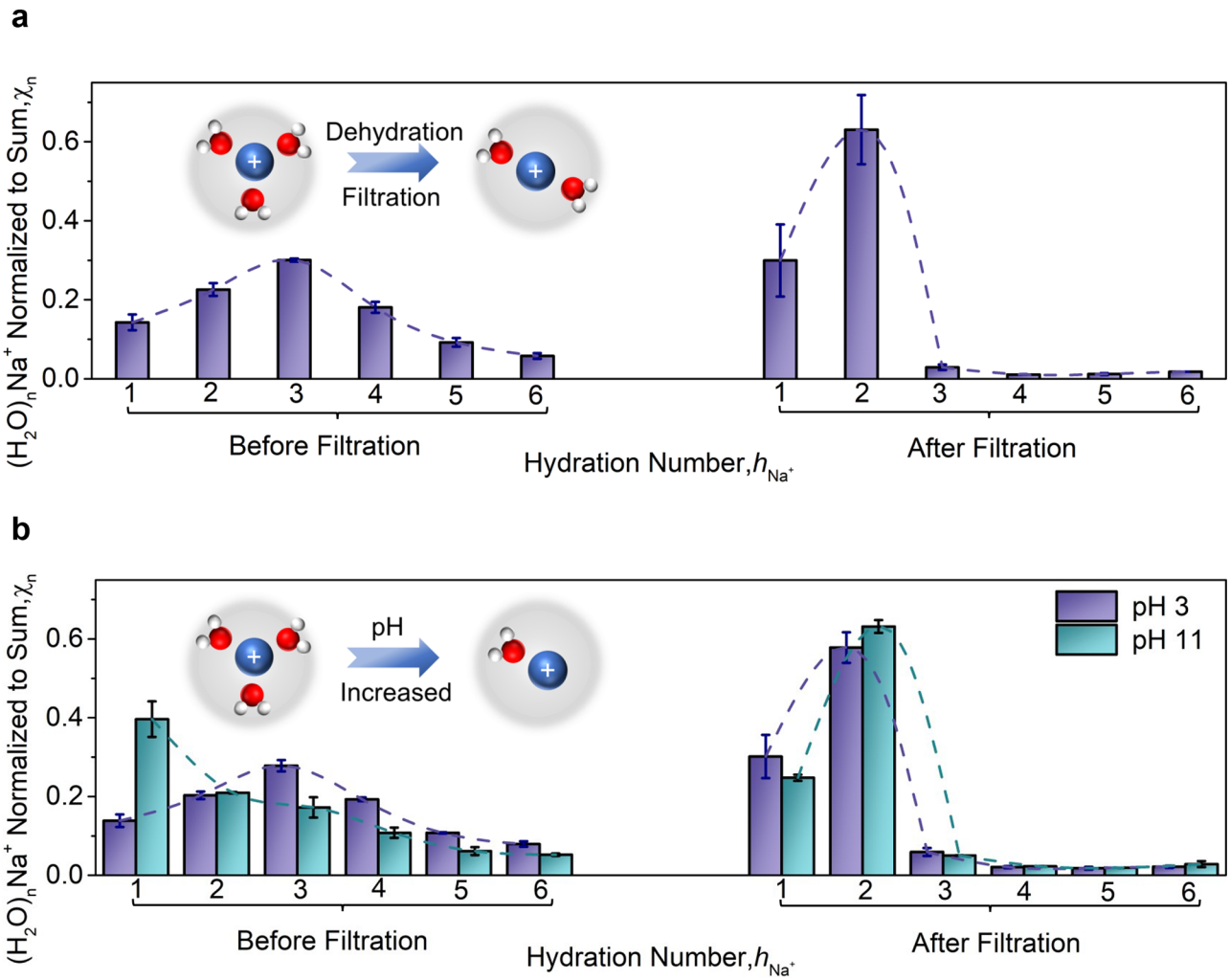

Figure 2. Variation of h_{Na+} distributions before and after filtration of NaCl solutions by NF90: (a) feed solution of 10 mM NaCl at pH 6.5; (b) feed solution of 10 mM NaCl at various pH values. The solution pH was adjusted with 1 M HCl and NaOH. The dotted lines in both panels are to guide the eye. Error bars represent standard deviations.

membrane and (ii) complete ion dehydration is not necessary for transport to occur.

Role of Steric Effects in Ion Dehydration. We investigated the role of steric effects on dehydration by analyzing the h_{Na+} distribution of sodium hydrates filtered by chemically similar membranes of varying pore size. Three nanofiltration membranes with nominal molecular weight cutoffs (MWCOs) of 200, 500, and 700 Da were selected (denoted as Trisep 1, Trisep 2, and Trisep 3, respectively). Trisep 1, Trisep 2, and NF90 all show a similar narrow pore size distribution (PSD), with mean effective pore radii of 0.29, 0.30, and 0.22 nm, respectively (details are given in Figure S6 in the Supporting Information). Trisep 3 presented a wider PSD, with an average estimated radius of 0.58 nm (Figure S6). The PSDs of our selected membranes represent the typical heterogeneous porous structures of polyamide films, which consist of intermolecular voids (radii smaller than ~3 Å) and some aggregate pores (radii between 3.5 and 4.5 Å).[53,54]

The average hydrated radius of a sodium ion (r_{H-Na^+}), estimated by corrections to the Stokes radius,[55] is 3.58 Å. We therefore postulate that dehydration must occur in the Trisep 1, Trisep 2, and NF90 membranes due to steric effects. Following our conjecture, the proportion of larger sodium hydrates (i.e., $\chi_{n\geq3}$) decreased from 0.63 to 0.14−0.15 after filtration by Trisep 1 and Trisep 2 (Figure S7a,b). Although it possesses an average pore radius larger than the average hydrated radius of sodium, Trisep 3 also induced some level of sodium dehydration, decreasing $\chi_{n\geq3}$ to 0.28 (Figure S7c). The ability of trihydrates to permeate the membrane was the largest difference between Trisep 3 and the tighter Trisep 1 and Trisep 2 membranes. The proportion of sodium hydrates with four or more water molecules decreased significantly (i.e., $\chi_{n\geq4}$) after they were filtered by the Trisep 3 membrane. We applied *ab initio* molecular dynamics (MD) simulations to estimate the size of the various sodium hydrates (see Figure S8 in the Supporting Information). Our simulations indicate that sodium hydrates with $h_{Na+} \geq 4$ have hydrated sizes smaller than the average size of the Trisep 3 pore (Table S2). This result suggests that mechanisms other than steric effects could lead to the absence of sodium hydrates with $h_{Na+} \geq 4$ after filtration by Trisep 3.

We included two additional alkali-metal ions, lithium (Li^+) and potassium (K^+), in our investigation (Figure 3a and Figure S9). Both Li^+ and K^+ are larger than the average pore size of the tight NF90 membrane (Figure S6), with hydrated radii of 3.82 and 3.31 Å, respectively.[55] Similarly to sodium hydrates, the proportion of the larger lithium and potassium hydrates (i.e., $\chi_{n\geq3}$) substantially decreased after filtration by NF90

https://doi.org/10.1021/jacs.1c05765
J. Am. Chem. Soc. 2021, 143, 14242−14252

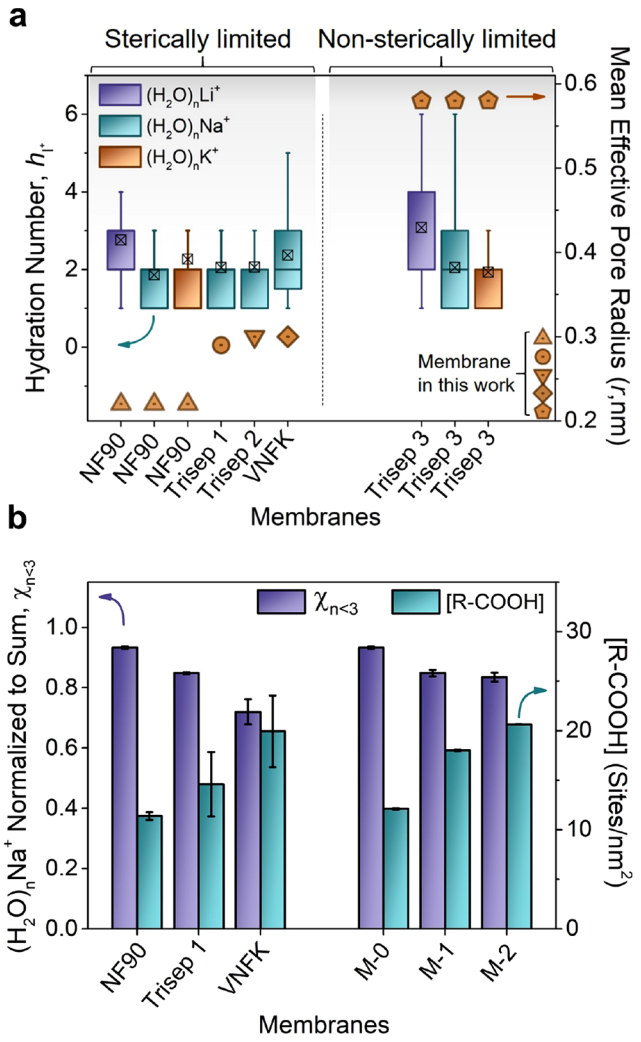

Figure 3. (a) Relationship between the hydration number distribution (h_{I^+}) and the mean effective pore radius of the polyamide membranes used in our study. The h_{I^+} value is presented with box plots based on Figure 2a and Figures S7, S9, and S11c, where the hatched square represents the mean h_{I^+} value. The pore size of the membranes can be divided into two groups: (i) sterically limited, where the pores are smaller than the traversing solvated ions (NF90, Trisep 1, Trisep 2 and VNFK), and (ii) non sterically limited, where the pores are larger than the traversing solvated ions (Trisep 3). (b) Relationship between R−COOH densities and the proportion of smaller hydrates (i.e., $\chi_{n<3}$) in the permeate after membrane filtration. The M-series membranes denote modified NF90 with various R−COOH densities: M-0 (12.10 sites nm^{-2}), M-1 (18.02 sites nm^{-2}), and M-2 (20.63 sites nm^{-2}). The total R−COOH density was quantified at pH 10.5. Error bars represent the standard deviations.

(Figure S9a,b). Li^+ surprisingly formed almost no monohydrates, $(H_2O)Li^+$, after filtration. The low proportion of lithium monohydrates ($\chi_{n=1}$ = 0.01) may be attributed to the abnormally low proportion of monohydrates in the bulk solution ($\chi_{n=1}$ = 0.04)—a likely consequence of Li^+'s high charge density and high hydration energy.[44] We also find that Li^+ and K^+ ions shift toward smaller hydrates in the non sterically limited Trisep 3 membrane (Figure 3a and Figure S9c,d), which had pores larger than the size of the hydrated ions. Regardless of the differences between these alkali-metal ions, dehydration appears to be ubiquitous when the pore size is commensurate with the hydrated size of the ion.

Mechanisms that could explain the shift toward smaller hydrates in non sterically limited transport are (i) low water permittivity in the pore and (ii) differences in the ionic mobilities of the hydrates. It has been widely established that low dielectric constants in polyamide membranes—driven by confinement effects—can significantly influence ion transport.[51,56,57] Specifically, the reduced polarizability of confined water molecules lessens the free solvation energy of the ion and hence its overall hydration capacity.[39,58,59] It is thus reasonable that the formation of hydrates with $h_{I^+} \geq 4$ would be unfavorable in low-dielectric environments. Our results also indicate that sodium monohydrates, $(H_2O)Na^+$, became the dominant species after filtering 10 mM NaCl through Trisep 3 (Figure S7c), with the proportion of each larger hydrate sequentially decreasing (i.e., $\chi_{n=1} > \chi_{n=2} > \chi_{n=3}$). This observation could be attributed to the difference in ionic mobilities of the various-sized sodium hydrates rather than dehydration. Ions with smaller solvation shells generally possess higher ionic mobility due to their compact structure, allowing for fast diffusion.[8,9,52,60] We therefore expect that smaller hydrates would diffuse more quickly across non sterically limited channels (i.e., channels that are larger than the size of the hydrated ion). Smaller hydrates would consequently show the highest signal when they are transported across the loose Trisep 3 membrane. This explanation is also consistent with previous work which showed that the selectivity of larger channels was governed by ionic mobilities.[10]

Influence of Viscous Effects during Transmembrane Transport. Viscous effects inside the nanochannels (e.g., due to electrostatic and van der Waals interactions) are another important factor affecting the confined transport of solvated ions.[13,61,62] These interactions may influence an ion's ability to partition into and diffuse across nanochannels due to physicochemical affinities with the pore mouth and wall. Notably, compensatory interactions between the ion and the pore wall could offset the penalty of dehydration and promote shedding or rearrangement of the solvation shell.[13]

We observe a slight difference in the proportion of smaller sodium hydrates (i.e., $\chi_{n<3}$) after filtering with membranes of similar pore size but different chemical characteristics (details are given in Figure S10 in the Supporting Information). Specifically, we see that $\chi_{n<3}$ = 0.933, 0.848, and 0.720 after filtration by NF90, Trisep 1, and VNFK, respectively (all polyamide membranes; Figure 3b). We quantified the total carboxyl group (R−COOH) density across the membrane—the primary charge contributor in polyamide nanofiltration membranes—to account for their chemical differences. We see an inverse trend in the R−COOH densities (Figure 3b), following the order VNFK (19.93 sites nm^{-2}) > Trisep 1 (14.60 sites nm^{-2}) > NF90 (11.38 sites nm^{-2}). We postulate that a stronger affinity between the smaller, more charge dense hydrates and negatively charged pores results in hindered diffusion,[47] consequently reducing the proportion of the smaller sodium hydrates (i.e., $\chi_{n<3}$) in the permeate.

To support our hypothesis, we modified NF90 to vary the R−COOH content (Figure S12), denoted as M-0 (12.10 sites nm^{-2}), M-1 (18.02 sites nm^{-2}), and M-2 (20.63 sites nm^{-2}). We find a negative correlation between $\chi_{n<3}$ and the R−COOH density of the M-series membranes (Figure 3b and Figure S13), validating the inverse relationship observed in the different commercial membranes. More importantly, this finding further suggests that higher densities of ionizable

https://doi.org/10.1021/jacs.1c05765
J. Am. Chem. Soc. 2021, 143, 14242−14252

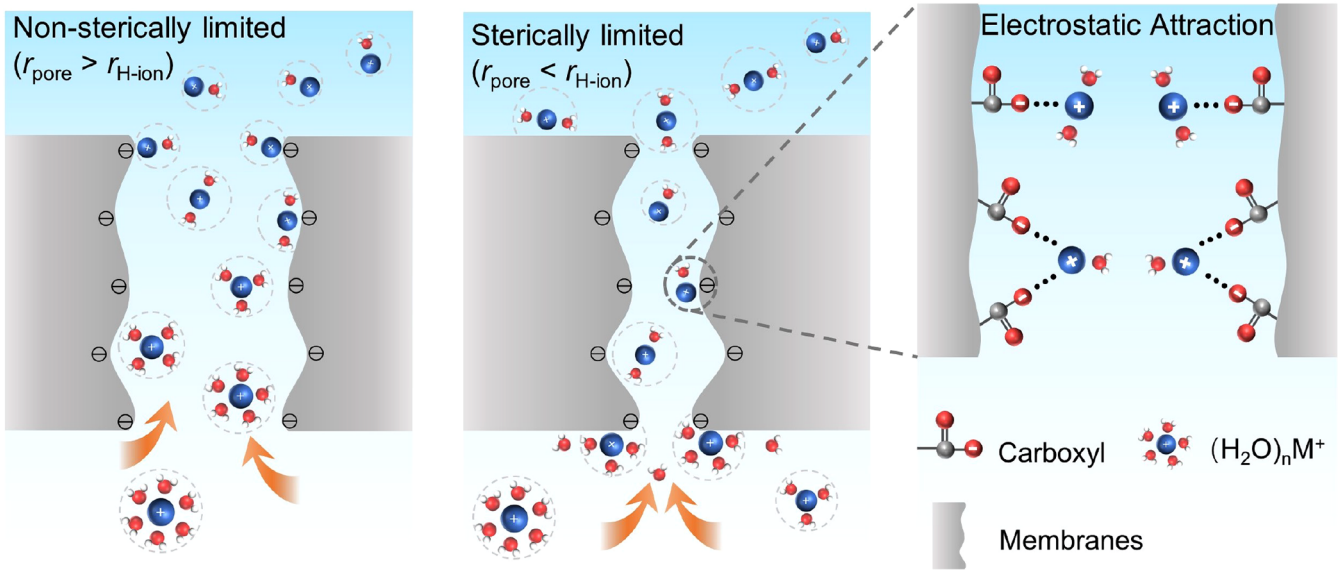

Figure 4. Schematic illustrations of the proposed ion transport mechanisms across polyamide membranes, represented as nanochannels for simplicity. When solvated ions are smaller than the size of the pore (left), transport is governed by ionic mobility. Conversely, dehydration dominates the transport of solvated ions larger than the size of the pore (middle). Viscous effects in the form of attractive ion−carboxyl interactions (right) can influence transport by hindering ionic mobility.

moieties such as R−COOH inside the nanochannels promote ion−wall interactions that can hinder ion transport and subsequently reduce the proportion of smaller, more charge dense solvated ions.

Our findings suggest that dehydration and viscous effects are key to the transmembrane transport of solvated ions. Figure 4 illustrates these transport mechanisms, highlighting the role of the nanoconduit size. In brief, we find that the transport of solvated ions larger than the membrane pore size is sterically limited, leading to an increased ToF-SIMS signal from smaller hydrates with narrow h_{I^-} distributions. Smaller hydrates also show an increased signal when the pore is larger than the solvated ions. Conversely, this results from differences in ionic mobilities of the hydrates and leads to broader h_{I^-} distributions. Viscous effects, resulting from ion−carboxyl group interactions, hinder the transport of solvated ions in both sterically and non sterically limited cases.

***In Silico* Investigation of Dehydration- and Viscosity-Based Transport Mechanisms.** We conducted MD simulations to study the transport behavior of solvated ions through model polyamide nanochannels of varying size and carboxyl density. The highly cross linked and void-like nature of polyamide's porous structure is difficult to model accurately. Therefore, we simplified the porous structure found in polyamide films to a nanochannel within the bulk polymer, as depicted in Figure 5a.[63] The bulk polymer was composed of repeating polyamide units, thus retaining the chemical properties of the polyamide which are essential to interactions between the membrane and solvated ion. A molecular representation of our MD simulations platform is depicted in Figure 5b.

Figure 5c shows the extracted h_{Na+} values during the simulated transport of sodium ions from bulk solution (i.e., feed solution) into the nanochannels. For sodium ions in the larger channel ($R \approx 0.5$ nm), the average h_{Na+} exhibited no observable difference from the bulk solution. In contrast, we find partial dehydration of sodium ions after they enter the smaller nanochannel ($R \approx 0.25$ nm) as the average h_{Na+} value decreased from ∼7 to ∼4 (Figure 5c and Figure S14a). These simulations support our experimental findings, which indicate that ion dehydration within the nanochannel does not require complete shedding of the solvation shell; rather, the solvation shell need only partially shed to enter the channel, similar to our experimental observations. To further understand this observation, we examined the radial distribution function (RDF) between Na^+ and the oxygen atoms of water (OW) as seen in Figure 5d. We find that only the 0.25 nm channel drives a distinct reduction in the OW density peak of the sodium ion's solvation layer. Our simulations therefore suggest that ion dehydration is only central to transport when the size of the nanochannel is smaller than the solvated ion, leading to water molecule shedding from the outermost solvation layer.

We analyzed the diffusion behavior of various sodium hydrates (h_{Na+} = 1−6) in the 0.5 nm channels in an effort to elucidate the mechanism governing the shift to smaller hydrates in non sterically limited transport. The diffusion coefficient of sodium ions (D_{Na+})—which directly relates to their ionic mobility—decreased monotonically as h_{Na+} increased (Figure S15a). The diffusion-driven flux of sodium (J_{Na^+}) was then calculated from D_{Na^+} (see Figure S15b in the Supporting Information). We find that the normalized diffusive flux (J_n), defined here as the flux of a single hydrate divided by the total flux of all hydrates (i.e., $J_n = J_{Na^+}/\sum J_{Na^+}$), decreases with increased h_{Na^+}. This trend coincides well with the relationship observed between χ_n and h_{Na^+} from ToF-SIMS (Figure 5e). This finding supports an ionic-mobility-based mechanism as the causal factor in the shift toward smaller hydrates in non sterically limited transport, such as sodium permeation across the Trisep 3 membrane. In other words, we see that the sodium ions with smaller solvation shells, which have a more compact structure, are able to diffuse across the larger nanochannels more rapidly. Higher mobility leads to a higher proportion of smaller hydrates being measured in the permeate (Figure S7c), consequently deviating from the normal-like distribution observed in bulk solution (Figure 2a).

https://doi.org/10.1021/jacs.1c05765
J. Am. Chem. Soc. 2021, 143, 14242−14252

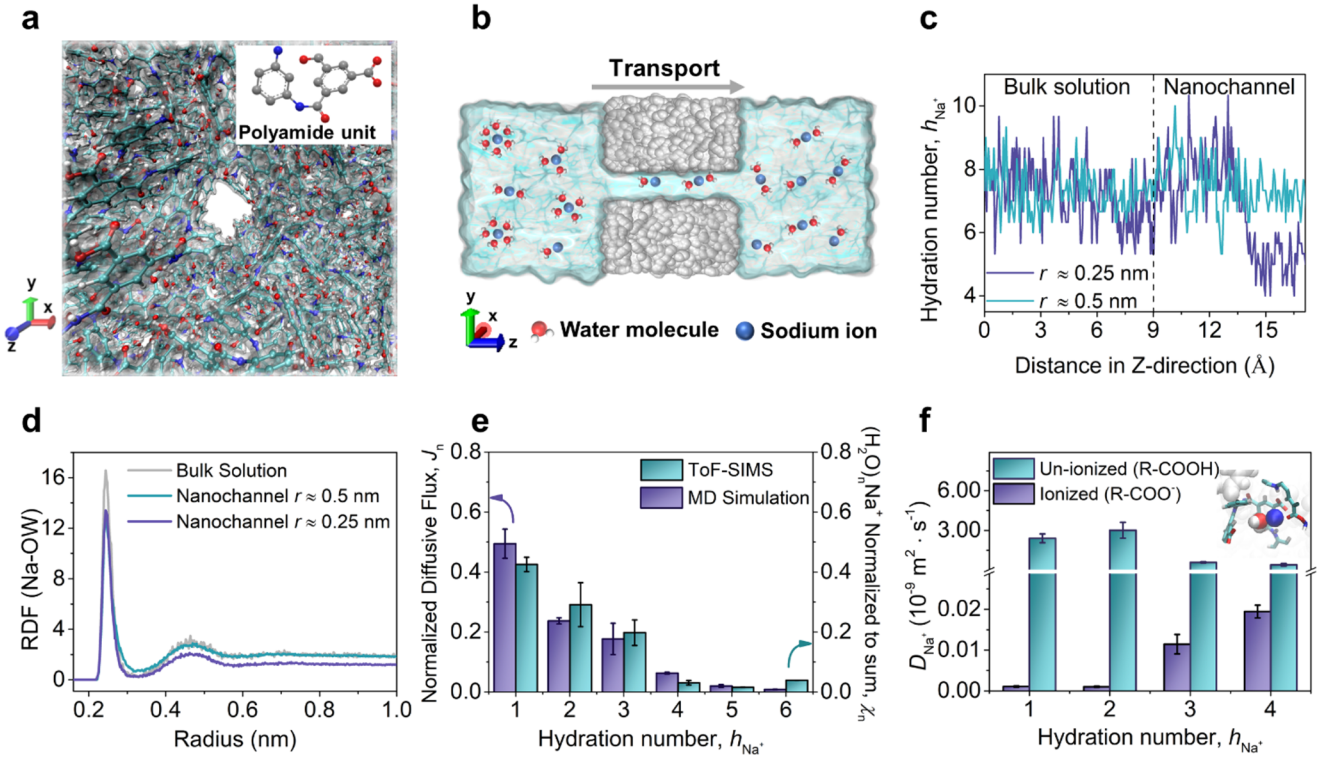

Figure 5. MD simulations of sodium ion transport across model polyamide nanochannels. (a) Simulated bulk polyamide with a nanochannel, where carbon, nitrogen, oxygen, and hydrogen atoms are represented in cyan, blue, red and white, respectively. The inset shows the repeating polyamide unit used to construct the bulk polymer. Carbon, nitrogen, and oxygen atoms are depicted as gray, blue, and red spheres, respectively, within the inset. (b) Cross-sectional illustration of the simulation platform. Ion transport was simulated across polyamide nanochannels connecting water-filled reservoirs with 0.04 M NaCl. The polyamide matrix material is depicted in gray. Na^+ ions are represented as blue spheres. (c) h_{Na+} as a function of distance in the Z direction from the bulk solution into the polyamide nanochannels. (d) Radial distribution function of water molecules bound to sodium ions in the bulk solutions and polyamide nanochannels. (e) Distribution of h_{Na+} after filtration of 10 mM NaCl by Trisep 3 (ToF-SIMS data from Figure S7c) compared with the relationship between the normalized diffusive flux (J_n; $J_n = J_{Na^+}/\sum J_{Na^+}$) and h_{Na^+} obtained from simulations. (f) Diffusion coefficients of sodium hydrates, D_{Na+}, confined within the smaller polyamide channel ($R \approx 0.25$ nm) of differing ionization states as a function of h_{Na+}. Polyamide ionization was controlled by modulating the protonation state of the carboxyl groups present: i.e., deprotonating un-ionized carboxylic acid groups (R−COOH) to their ionized state (R−COO$^-$). The inset depicts the formation of an ion pair between $(H_2O)Na^+$ and R−COO$^-$.

Finally, we employed our simulation platform to explore viscous effects arising from ion−carboxyl interactions in 0.25 nm channels. We selected only the smaller channel size, as the role of viscous interactions was expected to intensify under increased confinement. We find that D_{Na^+} decreased for all hydrates assessed (h_{Na^+} = 1−4) after ionizing the carboxyl groups (R−COO$^-$) in the polyamide nanochannel (Figure 5f). This decrease is attributable to the strong electrostatic interactions between ionogenic groups in confined environments.[39,64] In the ionized environment, D_{Na^+} saw greater decrements for small hydrates (i.e., $h_{Na^+} < 3$) than for large hydrates (i.e., $h_{Na^+} \geq 3$). This observation indicates that small hydrates experience more difficulty diffusing across ionized channels. Our simulations also reveal the formation of ion pairs between smaller sodium hydrates and R−COO$^-$ on the pore wall (details are given in Movie 1 in the Supporting Information). These *in silico* results support our initial hypothesis of hindered transport due to electrostatic interactions between Na^+ and R−COO$^-$ as well as the experimental findings in Figure 3b, which showed a reduced proportion of smaller sodium hydrates (i.e., $\chi_{n<3}$) corresponding to increased R−COO$^-$ density. While other viscous interactions (e.g., van der Waals forces) are likely at play, our results lead us to believe that electrostatic interactions are the most important.

CONCLUSION

This study presents the first *in situ* observation of changes in the hydration state of solvated ions following transport across extremely confined environments. The *operando* discrimination of ion solvation shells revealed a normal-like distribution for h_{I^+} of various alkali metal ions (Li^+, Na^+, and K^+) in bulk solution, with dihydrates and trihydrates as the predominant species. Filtration by sub-nanometer porous membranes induced ion dehydration for all species investigated. The shedding of water molecules from the solvation shell allowed ions to enter pores that were smaller than their bulk hydrated size. Notably, complete dehydration was not necessary for ion transport. Rather, solvated ions were able to traverse the membranes as smaller hydrates (i.e., $h_{I^+} < 3$ in our study) after partial dehydration. The proportion of these various hydrates measured in the permeate—which directly reflects their transport rate relative to all other hydrates—was largely influenced by the ion's response to steric confinement and viscous interactions (i.e., ion−carboxyl interactions). MD simulations supported our experimental findings; specifically, our *in silico* analyses demonstrate that differences in the ionic

https://doi.org/10.1021/jacs.1c05765
J. Am. Chem. Soc. 2021, 143, 14242−14252

mobility of various hydrates is central to ion transport in channels larger than the size of the solvated ions. MD simulations also confirmed that the ionization of carboxyl groups within polyamide nanochannels hinders ion transport via enhanced electrostatics.

The establishment of *in situ* liquid ToF-SIMS as a new experimental technique to obtain dynamic information regarding the structure of solvated ions enables novel investigatory science in nanofluidics and other related fields. Understanding the mechanisms of confined ion transport is paramount to developing highly selective membranes as well as advancing other applications of nanofluidics, such as biosensing, energy conversion, and battery development. Our work highlights the importance of the physical and chemical properties of the membrane pore to ion dehydration. We envision that future studies and membrane design focusing on dehydration-dominated transport, while the influence of viscous effects is also considered, will lead to significant advancements in our fundamental understanding of nanoconfined transport and the field of nanofluidics.

EXPERIMENTAL SECTION

Chemicals and Materials. Electrolyte solutions were prepared in deionized water (DI, Millipore Milli-Q). Sodium chloride (NaCl, ≥99.9%), potassium chloride (KCl, ≥99.9%), lithium chloride (LiCl, ≥99.9%), sodium hydroxide (NaOH, ≥99.9%), polytetrafluoroethylene (PTFE), and polydimethylsiloxane (PDMS) were purchased from Sigma-Aldrich (St. Louis, MO, USA). Hydrochloric acid (HCl, 36−38%), ethylene glycol ($C_2H_6O_2$, ≥99%), glycerol ($C_3H_8O_3$, ≥99%), diethylene glycol ($C_4H_{10}O_3$, ≥99%), polyethylene glycol (PEG, ≥99%, MWs of 200, 400, 600, 800, and 1000 Da), acrylic acid ($C_3H_4O_2$, ≥99%), potassium persulfate ($K_2S_2O_8$, ≥99%), sodium pyrosulfite ($Na_2S_2O_5$, ≥99%), silver nitrate ($AgNO_3$, ≥99%), and nitric acid (HNO_3, 65−68%) were obtained from Sinopharm Chemical Regent Co., Ltd., China. The silicon nitride (SiN_x) film (Norcada Inc., Edmonton, Canada) was used as the detective window. One molar NaOH and HCl were used to adjust the solution pH in experiments. NF90, Trisep (1−3), and VNFK nanofiltration membranes were purchased from DOW FilmTec chemical company (USA), MICRODYN-NADIR (Germany), and VONTRON (China), respectively.

Fabrication of Microfluidic Filtration Device. The fabrication of the microfluidic chip used for *in situ* liquid ToF-SIMS has been reported elsewhere.[31,33,34] In brief, a 200 μm × 300 μm (width × depth) channel was made by soft lithography in a polydimethylsiloxane (PDMS) block. The SiN_x film (100 nm in thickness) supported on a silicon frame (window size 0.5 mm × 0.5 mm) was irreversibly bonded with the PDMS block by air plasma to form the detection area. The membrane was deliberately sealed between the electrolyte feed solution and SiN_x film with an epoxy glue. The membrane active (selective) layer faced the vacuum side to avoid the rehydration of ions.

Analysis by *In Situ* Liquid ToF-SIMS. The detection procedure of the hydration number distribution was performed with a ToF-SIMS V instrument (IONTOF GmbH, Münster, Germany) equipped with a bismuth liquid metal ion gun. A pulsed 30 keV Bi_3^+ primary ion beam in positive mode was focused to a lateral resolution of ∼250 nm (details in Figure S17), and the charge was neutralized by a 20 eV electron flood gun. During SiN_x perforation, the pulse width was 160 ns and the current was ∼0.30 pA. Once the SiN_x film was completely punched through, the pulse width and the current were immediately adjusted to 80 ns and ∼0.12 pA, respectively, for a higher mass resolution. Specifically, the mass resolution was increased from ∼99 to ∼320 after SiN_x perforation. We also note that the reduction in pulse width will not change the focus of the ion beam; thus, the lateral resolution remains at ∼250 nm for the entire analysis. The analysis area during mass spectrometry was ∼2 μm in diameter. The integration time for each measurement was ∼800 s. The ultrahigh-vacuum pressure differential across the membrane drove permeation of the electrolyte solution from the feed side to the vacuum chamber. The mass spectrum signals of the electrolyte solution were collected instantly after permeating across the membrane, allowing for a direct analysis of the hydration number distribution with high temporal and spatial resolution. We carried out the same experiment in the microfluidic device with no membrane to collect the hydration number distribution prior to filtration. All experiments were repeated in triplicate. Details of the data processing are provided in the Supporting Information.

Device and Membrane Characterization. The membrane-sealed microfluidic chip was sputter-coated with platinum for scanning electron microscopy (SEM, JSM7401F, JEDL, Japan) to investigate the analysis area after Bi_3^+ primary ion bombardment. Energy dispersive X-ray spectroscopy (EDS, IXRF Model 550i, USA) was utilized to assess differences in the elementary composition inside and outside of the analysis area. Membrane pore size distributions were estimated using inert solutes and the pore transport model.[65−67] The neutral organic molecules used in this method were measured with a total organic carbon (TOC) analyzer (TOC-VCPH, Shimadzu, Japan). On the basis of the bind-and-elute method,[50] we utilized silver ion probes to measure ionized carboxyl densities within the polyamide films. Eluted silver was quantified using inductively coupled plasma mass spectrometry (ICP-MS,7500a, Agilent Technologies Inc., USA). We modified the carboxyl densities of our membranes via radical grafting.[68] The chemical components of the membrane were investigated by performing attenuated total reflectance Fourier transform infrared (ATR-FTIR, Nicolet 8700, Thermo Fisher Scientific) and X-ray photoelectron spectroscopy (XPS, ESCALAB 250Xi, Thermo Fisher Scientific, USA). More details on the characterization methods used in this study are described in the Supporting Information.

Molecular Dynamics Simulations. The MD simulations were performed using the GROMACS 5.1.2 software.[69] The amber99SB force field[70] was used to describe the polyamide polymer with the tip3p water model[71] for solvent molecules. The temperature of water and polyamide was kept constant, coupling independently for each group of molecules at 300 K with a V-rescale thermostat.[72] The pressure was coupled with a Parrinello−Rahman[73] barostat at 1 atm separately in each of the three dimensions. The temperature and pressure time constants of the coupling were 0.1 and 2 ps, respectively. The integration of the equations of motion was performed by using a leapfrog algorithm with a time step of 2 fs. Periodic boundary conditions were implemented in all systems. A cutoff of 1 nm was implemented for the Lennard−Jones interactions and for the direct space part of the Ewald sum for Coulombic interactions. The Fourier space part of the Ewald splitting was computed by using the particle-mesh-Ewald method,[74] with a grid length of 0.16 nm and a cubic spline interpolation. Additional details on the simulation platform, calculations, and parameters are described in the Supporting Information.

ASSOCIATED CONTENT

Supporting Information

The Supporting Information is available free of charge at https://pubs.acs.org/doi/10.1021/jacs.1c05765.

MD trajectory of monohydrated sodium ion through the 338 ionized polyamide nanochannel (MPG)

Details of ToF-SIMS data processing, pore size distribution measurement, characterizing polyamide functional groups, membrane carboxylation via grafting, molecular dynamics simulations, and ion pair formation (PDF)

https://doi.org/10.1021/jacs.1c05765
J. Am. Chem. Soc. 2021, 143, 14242−14252

AUTHOR INFORMATION

Corresponding Authors

Chengzhi Hu − *State Key Laboratory of Environmental Aquatic Chemistry, Research Center for Eco-Environmental Sciences, Chinese Academy of Sciences, Beijing 100085, People's Republic of China; University of Chinese Academy of Sciences, Beijing 100049, People's Republic of China;* orcid.org/0000-0001-9898-835X; Email: czhu@rcees.ac.cn

Menachem Elimelech − *Department of Chemical and Environmental Engineering, Yale University, New Haven, Connecticut 06520, United States;* orcid.org/0000-0003-4186-1563; Email: meachem.elimelech@yale.edu

Jiuhui Qu − *State Key Laboratory of Environmental Aquatic Chemistry, Research Center for Eco-Environmental Sciences, Chinese Academy of Sciences, Beijing 100085, People's Republic of China; University of Chinese Academy of Sciences, Beijing 100049, People's Republic of China;* orcid.org/0000-0001-9177-093X; Email: jhqu@rcees.ac.cn

Authors

Chenghai Lu − *State Key Laboratory of Environmental Aquatic Chemistry, Research Center for Eco-Environmental Sciences, Chinese Academy of Sciences, Beijing 100085, People's Republic of China; University of Chinese Academy of Sciences, Beijing 100049, People's Republic of China*

Cody L. Ritt − *Department of Chemical and Environmental Engineering, Yale University, New Haven, Connecticut 06520, United States;* orcid.org/0000-0002-3215-1685

Xin Hua − *School of Chemistry and Molecular Engineering, East China University of Science and Technology, Shanghai 200237, People's Republic of China*

Jingqiu Sun − *State Key Laboratory of Environmental Aquatic Chemistry, Research Center for Eco-Environmental Sciences, Chinese Academy of Sciences, Beijing 100085, People's Republic of China; University of Chinese Academy of Sciences, Beijing 100049, People's Republic of China*

Hailun Xia − *School of Chemistry and Molecular Engineering, East China University of Science and Technology, Shanghai 200237, People's Republic of China*

Yingya Liu − *School of Chemistry and Molecular Engineering, East China University of Science and Technology, Shanghai 200237, People's Republic of China*

Da-Wei Li − *School of Chemistry and Molecular Engineering, East China University of Science and Technology, Shanghai 200237, People's Republic of China;* orcid.org/0000-0002-9257-4452

Baiwen Ma − *State Key Laboratory of Environmental Aquatic Chemistry, Research Center for Eco-Environmental Sciences, Chinese Academy of Sciences, Beijing 100085, People's Republic of China; University of Chinese Academy of Sciences, Beijing 100049, People's Republic of China;* orcid.org/0000-0003-2343-615X

Complete contact information is available at: https://pubs.acs.org/10.1021/jacs.1c05765

Author Contributions

All authors have given approval to the final version of the manuscript.

Funding

This work was supported by the National Natural Science Foundation of China (51978646 and 51738013), the Chinese Academy of Sciences, Key Research Program of Frontier Sciences (ZDBS-LYDQC014) and the ,Excellent Innovation Project of Research Center for Eco-Environmental Sciences (RCEES-EEI-2019-02). We also acknowledge support from the United States National Science Foundation, Division of Graduate Education (DGE1752134) for C.L.R. and Division of Chemical, Bioengineering, Environmental, and Transport Systems (CBET-2001219) for M.E.

Notes

The authors declare no competing financial interest.

ACKNOWLEDGMENTS

We would like to greatly thank that team of Prof. Yi-Tao Long at East China University of Science and Technology, provided the pore-confined devices and methods for *in situ* liquid ToF-SIMS analysis. We are grateful to Yan Jin, Song-Miao Liang and Yan Kang from VONTRON Technology Co., LTD, for their technical support in membrane preparation. We also thank Feng Zhou at Nanyang Technological University, Singapore for his help with the MD simulations.

REFERENCES

(1) Gouaux, E.; Mackinnon, R. Principles of selective ion transport in channels and pumps. *Science* **2005**, *310* (5753), 1461−5.

(2) Hou, X.; Guo, W.; Jiang, L. Biomimetic smart nanopores and nanochannels. *Chem. Soc. Rev.* **2011**, *40* (5), 2385−401.

(3) Chen, L.; Shi, G.; Shen, J.; Peng, B.; Zhang, B.; Wang, Y.; Bian, F.; Wang, J.; Li, D.; Qian, Z.; Xu, G.; Liu, G.; Zeng, J.; Zhang, L.; Yang, Y.; Zhou, G.; Wu, M.; Jin, W.; Li, J.; Fang, H. Ion sieving in graphene oxide membranes via cationic control of interlayer spacing. *Nature* **2017**, *550* (7676), 380−383.

(4) Kopec, W.; Kopfer, D. A.; Vickery, O. N.; Bondarenko, A. S.; Jansen, T. L. C.; de Groot, B. L.; Zachariae, U. Direct knock-on of desolvated ions governs strict ion selectivity in K^+ channels. *Nat. Chem.* **2018**, *10* (8), 813−820.

(5) Schoch, R. B.; et al. Transport phenomena in nanofluidics. *Rev. Mod. Phys.* **2008**, *80*, 839−883.

(6) Peng, J.; Cao, D.; He, Z.; Guo, J.; Hapala, P.; Ma, R.; Cheng, B.; Chen, J.; Xie, W. J.; Li, X.-Z.; Jelínek, P.; Xu, L.-M.; Gao, Y. Q.; Wang, E.-G.; Jiang, Y. The effect of hydration number on the interfacial transport of sodium ions. *Nature* **2018**, *557* (7707), 701−705.

(7) Payandeh, J.; Scheuer, T.; Zheng, N.; Catterall, W. A. The crystal structure of a voltage-gated sodium channel. *Nature* **2011**, *475* (7356), 353−8.

(8) Zhang, H.; Hou, J.; Hu, Y.; Wang, P.; Ou, R.; Jiang, L.; Liu, J. Z.; Freeman, B. D.; Hill, A. J.; Wang, H. Ultrafast selective transport of alkali metal ions in metal organic frameworks with subnanometer pores. *Sci. Adv.* **2018**, *4* (2), eaaq0066.

(9) Wen, Q.; Yan, D.; Liu, F.; Wang, M.; Ling, Y.; Wang, P.; Kluth, P.; Schauries, D.; Trautmann, C.; Apel, P.; Guo, W.; Xiao, G.; Liu, J.; Xue, J.; Wang, Y. Highly selective ionic transport through subnanometer pores in polymer films. *Adv. Funct. Mater.* **2016**, *26* (32), 5796−5803.

(10) Wang, P.; Wang, M.; Liu, F.; Ding, S.; Wang, X.; Du, G.; Liu, J.; Apel, P.; Kluth, P.; Trautmann, C.; Wang, Y. Ultrafast ion sieving using nanoporous polymeric membranes. *Nat. Commun.* **2018**, *9* (1), 569.

(11) Wang, M.; Shen, W.; Ding, S.; Wang, X.; Wang, Z.; Wang, Y.; Liu, F. A coupled effect of dehydration and electrostatic interactions on selective ion transport through charged nanochannels. *Nanoscale* **2018**, *10* (39), 18821−18828.

(12) Porter, C. J.; Werber, J. R.; Zhong, M.; Wilson, C. J.; Elimelech, M. Pathways and challenges for biomimetic desalination membranes

with sub-nanometer channels. *ACS Nano* **2020**, *14* (9), 10894−10916.
(13) Epsztein, R.; DuChanois, R. M.; Ritt, C. L.; Noy, A.; Elimelech, M. Towards single-species selectivity of membranes with subnanometre pores. *Nat. Nanotechnol.* **2020**, *15* (6), 426−436.
(14) Sahu, S.; Di Ventra, M.; Zwolak, M. Dehydration as a universal mechanism for ion selectivity in graphene and other atomically thin pores. *Nano Lett.* **2017**, *17* (8), 4719−4724.
(15) Zhou, K.; Xu, Z. Renormalization of ionic solvation shells in nanochannels. *ACS Appl. Mater. Interfaces* **2018**, *10* (33), 27801−27809.
(16) Zhou, K.; Xu, Z. Ion permeability and selectivity in composite nanochannels: engineering through the end effects. *J. Phys. Chem. C* **2020**, *124* (8), 4890−4898.
(17) Daiguji, H. Ion transport in nanofluidic channels. *Chem. Soc. Rev.* **2010**, *39* (3), 901−11.
(18) Corry, B. Mechanisms of selective ion transport and salt rejection in carbon nanostructures. *MRS Bull.* **2017**, *42* (04), 306−310.
(19) Richards, L. A.; Schafer, A. I.; Richards, B. S.; Corry, B. The importance of dehydration in determining ion transport in narrow pores. *Small* **2012**, *8* (11), 1701−9.
(20) Corry, B. Water and ion transport through functionalised carbon nanotubes: implications for desalination technology. *Energy Environ. Sci.* **2011**, *4* (3), 751.
(21) Zhang, Z.; Sui, X.; Li, P.; Xie, G.; Kong, X. Y.; Xiao, K.; Gao, L.; Wen, L.; Jiang, L. Ultrathin and ion-selective janus membranes for high-performance osmotic energy conversion. *J. Am. Chem. Soc.* **2017**, *139* (26), 8905−8914.
(22) Zhu, Z.; Wang, D.; Tian, Y.; Jiang, L. Ion/molecule transportation in nanopores and nanochannels: from critical principles to diverse functions. *J. Am. Chem. Soc.* **2019**, *141* (22), 8658−8669.
(23) Patel, S. K.; Ritt, C. L.; Deshmukh, A.; Wang, Z.; Qin, M.; Epsztein, R.; Elimelech, M. The relative insignificance of advanced materials in enhancing the energy efficiency of desalination technologies. *Energy Environ. Sci.* **2020**, *13* (6), 1694−1710.
(24) Miyazaki, M.; Fujii, A.; Ebata, T.; Mikami, N. Infrared spectroscopic evidence for protonated water clusters forming nanoscale cages. *Science* **2004**, *304* (5674), 1134−7.
(25) Luo, Z. X.; Xing, Y. Z.; Liu, S.; Ling, Y. C.; Kleinhammes, A.; Wu, Y. Dehydration of ions in voltage-gated carbon nanopores observed by in situ NMR. *J. Phys. Chem. Lett.* **2015**, *6* (24), 5022−6.
(26) Ohba, T.; Hata, K.; Kanoh, H. Significant hydration shell formation instead of hydrogen bonds in nanoconfined aqueous electrolyte solutions. *J. Am. Chem. Soc.* **2012**, *134* (43), 17850−3.
(27) Scatena, L. F.; Brown, M. G.; Richmond, G. L. Water at hydrophobic surfaces: weak hydrogen bonding and strong orientation effects. *Science* **2001**, *292* (5518), 908−12.
(28) Ohkubo, T.; Konishi, T.; Hattori, Y.; Kanoh, H.; Fujikawa, T.; Kaneko, K. Restricted hydration structures of Rb and Br ions confined in slit-shaped carbon nanospace. *J. Am. Chem. Soc.* **2002**, *124*, 11860−11861.
(29) Zhou, Y.; Yao, J.; Ding, Y.; Yu, J.; Hua, X.; Evans, J. E.; Yu, X.; Lao, D. B.; Heldebrant, D. J.; Nune, S. K.; Cao, B.; Bowden, M. E.; Yu, X.-Y.; Wang, X.-L.; Zhu, Z. Improving the molecular ion signal intensity for in situ liquid SIMS analysis. *J. Am. Soc. Mass Spectrom.* **2016**, *27* (12), 2006−2013.
(30) Benninghoven, A. Chemical analysis of inorganic and organic surfaces and thin films by static time-of-flight secondary ion mass spectrometry (TOF-SIMS). *Angew. Chem., Int. Ed. Engl.* **1994**, *33*, 1023−1043.
(31) Zhang, Y.; Zeng, W.; Huang, L.; Liu, W.; Jia, E.; Zhao, Y.; Wang, F.; Zhu, Z. In situ liquid secondary ion mass spectrometry: a surprisingly soft ionization process for investigation of halide ion hydration. *Anal. Chem.* **2019**, *91* (11), 7039−7046.
(32) Zhou, Y. F.; Su, M.; Yu, X. F.; Zhang, Y. Y.; Wang, J. G.; Ren, X. D.; Cao, R. G.; Xu, W.; Baer, D. R.; Du, Y. G.; Borodin, O.; Wang, Y. T.; Wang, X. L.; Xu, K.; Xu, Z. J.; Wang, C. M.; Zhu, Z. H. Real-time mass spectrometric characterization of the solid-electrolyte interphase of a lithium-ion battery. *Nat. Nanotechnol.* **2020**, *15* (3), 224−230.
(33) Liu, Y.-Y.; Ying, Y.-L.; Hua, X.; Long, Y.-T. In-situ discrimination of the water cluster size distribution in aqueous solution by ToF-SIMS. *Sci. China: Chem.* **2018**, *61* (2), 159−163.
(34) Liu, Y.-Y.; Zhang, S.-Z.; Ying, Y.-L.; Xia, H.-L.; Hua, X.; Long, Y.-T. Ion-specific effects on hydrogen bond network at a submicropore confined liquid-vacuum interface: an in situ liquid ToF-SIMS study. *J. Phys. Chem. Lett.* **2019**, *10* (17), 4935−4941.
(35) Yuan, G.; Zhou, J. Electrospray ionization mass spectral fragmentation mechanisms of DNA-recognizing polyamides containing N-methylpyrrole and N-methylimidazol. *Rapid Commun. Mass Spectrom.* **2004**, *18* (12), 1397−402.
(36) Tang, C. Y. Y.; Kwon, Y. N.; Leckie, J. O. Effect of membrane chemistry and coating layer on physiochemical properties of thin film composite polyamide RO and NF membranes I. FTIR and XPS characterization of polyamide and coating layer chemistry. *Desalination* **2009**, *242* (1−3), 149−167.
(37) Ohtaki, H.; Radnai, T. Structure and dynamics of hydrated ions. *Chem. Rev.* **1993**, *93* (3), 1157−1204.
(38) Rode, B. M.; Schwenk, C. F.; Hofer, T. S.; Randolf, B. R. Coordination and ligand exchange dynamics of solvated metal ions. *Coord. Chem. Rev.* **2005**, *249* (24), 2993−3006.
(39) Marcus, Y. *Ions in solution and their solvation*; Wiley: 2015.
(40) Marcus, Y. Electrostriction, ion solvation, and solvent release on ion pairing. *J. Phys. Chem. B* **2005**, *109* (39), 18541−18549.
(41) Bockris, J. O. M.; Saluja, P. P. S. Ionic solvation numbers from compressibilities and ionic vibration potentials measurements. *J. Phys. Chem.* **1972**, *76* (15), 2140−2151.
(42) Marcus, Y. The standard partial molar volumes of ions in solution. Part 4. Ionic volumes in water at 0−100 degrees C. *J. Phys. Chem. B* **2009**, *113* (30), 10285−10291.
(43) Hilal, N.; Al-Zoubi, H.; Darwish, N. A.; Mohammad, A. W. Characterisation of nanofiltration membranes using atomic force microscopy. *Desalination* **2005**, *177* (1−3), 187−199.
(44) Hribar, B.; Southall, N. T.; Vlachy, V.; Dill, K. A. How ions affect the structure of water. *J. Am. Chem. Soc.* **2002**, *124* (44), 12302−12311.
(45) Huisken, F.; Kaloudis, M.; Kulcke, A. Infrared spectroscopy of small size-selected water clusters. *J. Chem. Phys.* **1996**, *104*, 17−25.
(46) Liu, K.; Brown, M. G.; Carter, C.; Saykally, R. J.; Gregory, J. K.; Clary, D. C. Characterization of a cage form of the water hexamer. *Nature* **1996**, *381*, 501−503.
(47) Zhou, X.; Wang, Z.; Epsztein, R.; Zhan, C.; Li, W.; Fortner, J. D.; Pham, T. A.; Kim, J.-H.; Elimelech, M. Intrapore energy barriers govern ion transport and selectivity of desalination membranes. *Sci. Adv.* **2020**, *6*, eabd9045.
(48) Moldenhauer, H.; Diaz-Franulic, I.; Gonzalez-Nilo, F.; Naranjo, D. Effective pore size and radius of capture for K^+ ions in K-channels. *Sci. Rep.* **2016**, *6*, 19893.
(49) Helfferich, F. *Ion Exchange*; McGraw-Hill: 1962.
(50) Chen, D.; Werber, J. R.; Zhao, X.; Elimelech, M. A facile method to quantify the carboxyl group areal density in the active layer of polyamide thin-film composite membranes. *J. Membr. Sci.* **2017**, *534*, 100−108.
(51) Ritt, C. L.; Werber, J. R.; Wang, M.; Yang, Z.; Zhao, Y.; Kulik, H. J.; Elimelech, M. Ionization behavior of nanoporous polyamide membranes. *Proc. Natl. Acad. Sci. U. S. A.* **2020**, *117* (48), 30191−30200.
(52) Song, C.; Corry, B. Intrinsic ion selectivity of narrow hydrophobic pores. *J. Phys. Chem. B* **2009**, *113* (21), 7642−9.
(53) Wei, T.; Zhang, L.; Zhao, H.; Ma, H.; Sajib, M. S.; Jiang, H.; Murad, S. Aromatic polyamide reverse-osmosis membrane: an atomistic molecular dynamics simulation. *J. Phys. Chem. B* **2016**, *120* (39), 10311−10318.
(54) Kim, S. H.; Kwak, S.-Y.; Suzuki, T. Positron annihilation spectroscopic evidence to demonstrate the flux-enhancement mechanism in morphology-controlled thin-film-composite (TFC) membrane. *Environ. Sci. Technol.* **2005**, *39*, 1764−1770.

https://doi.org/10.1021/jacs.1c05765
J. Am. Chem. Soc. 2021, 143, 14242−14252

(55) Nightingale, E. R. Phenomenological theory of ion solvation. Effective radii of hydrated ions. *J. Phys. Chem.* **1959**, *63* (9), 1381−1387.
(56) Freger, V. Ion partitioning and permeation in charged low-T* membranes. *Adv. Colloid Interface Sci.* **2020**, *277*, 102107.
(57) Szymczyk, A.; Fievet, P. Investigating transport properties of nanofiltration membranes by means of a steric, electric and dielectric exclusion model. *J. Membr. Sci.* **2005**, *252* (1−2), 77−88.
(58) Born, M. Volumen und hydratationswärme der ionen. *Eur. Phys. J. A* **1920**, *1* (1), 45−48.
(59) Duignan, T. T.; Zhao, X. S. The Born model can accurately describe electrostatic ion solvation. *Phys. Chem. Chem. Phys.* **2020**, *22* (43), 25126−25135.
(60) Li, L.; Dong, J.; Nenoff, T. Transport of water and alkali metal ions through MFI zeolite membranes during reverse osmosis. *Sep. Purif. Technol.* **2007**, *53* (1), 42−48.
(61) Choi, W.; Ulissi, Z. W.; Shimizu, S. F.; Bellisario, D. O.; Ellison, M. D.; Strano, M. S. Diameter-dependent ion transport through the interior of isolated single-walled carbon nanotubes. *Nat. Commun.* **2013**, *4*, 2397.
(62) Eyring, H. Viscosity, plasticity, and diffusion as examples of absolute reaction rates. *J. Chem. Phys.* **1936**, *4* (4), 283−291.
(63) Cruz-Chu, E. R.; Ritz, T.; Siwy, Z. S.; Schulten, K. Molecular control of ionic conduction in polymer nanopores. *Faraday Discuss.* **2009**, *143*, 47−62.
(64) Yaroshchuk, A. E. Dielectric exclusion of ions from membranes. *Adv. Colloid Interface Sci.* **2000**, *85* (2−3), 193−230.
(65) Otero, J. A.; Mazarrasa, O.; Villasante, J.; Silva, V.; Prádanos, P.; Calvo, J. I.; Hernández, A. Three independent ways to obtain information on pore size distributions of nanofiltration membranes. *J. Membr. Sci.* **2008**, *309* (1−2), 17−27.
(66) García-Martín, N.; Silva, V.; Carmona, F. J.; Palacio, L.; Hernández, A.; Prádanos, P. Pore size analysis from retention of neutral solutes through nanofiltration membranes. The contribution of concentration−polarization. *Desalination* **2014**, *344*, 1−11.
(67) Wang, K.; Chung, T. Fabrication of polybenzimidazole (PBI) nanofiltration hollow fiber membranes for removal of chromate. *J. Membr. Sci.* **2006**, *281* (1−2), 307−315.
(68) Belfer, S.; Purinson, Y.; Kedem, O. Surface modification of commercial polyamide reverse osmosis membranes by radical grafting: an ATR-FTIR study. *Acta Polym.* **1998**, *49*, 574−582.
(69) Van Der Spoel, D.; Lindahl, E.; Hess, B.; Groenhof, G.; Mark, A. E.; Berendsen, H. J. GROMACS: fast, flexible, and free. *J. Comput. Chem.* **2005**, *26* (16), 1701−1718.
(70) Huang, J.; Rauscher, S.; Nawrocki, G.; Ran, T.; Feig, M.; de Groot, B. L.; Grubmüller, H.; MacKerell, A. D. CHARMM36m: an improved force field for folded and intrinsically disordered proteins. *Nat. Methods* **2017**, *14* (1), 71−73.
(71) Mackerell, A. D., Jr; Feig, M.; Brooks III, C. L. Extending the treatment of backbone energetics in protein force fields: limitations of gas-phase quantum mechanics in reproducing protein conformational distributions in molecular dynamics simulations. *J. Comput. Chem.* **2004**, *25* (11), 1400−1415.
(72) Bussi, G.; Donadio, D.; Parrinello, M. Canonical sampling through velocity rescaling. *J. Chem. Phys.* **2007**, *126* (1), 014101.
(73) Parrinello, M.; Rahman, A. Polymorphic transitions in single crystals: a new molecular dynamics method. *J. Appl. Phys.* **1981**, *52* (12), 7182−7190.
(74) Darden, T.; York, D.; Pedersen, L. Particle mesh Ewald: an N·log (N) method for Ewald sums in large systems. *J. Chem. Phys.* **1993**, *98* (12), 10089−10092.

https://doi.org/10.1021/jacs.1c05765
J. Am. Chem. Soc. 2021, 143, 14242−14252